ACS Catalysis

Research Article

pubs.acs.org/acscatalysis

Enhancement of the Hydrogen Evolution Reaction from Ni-MoS_2 Hybrid Nanoclusters

Daniel Escalera-López,[†,‡] Yubiao Niu,[‡] Jinlong Yin,[§] Kevin Cooke,[§] Neil V. Rees,*[,†] and Richard E. Palmer*[,‡]

[†]Centre for Hydrogen and Fuel Cell Research, School of Chemical Engineering, University of Birmingham, Birmingham B15 2TT, United Kindgom

[‡]Nanoscale Physics Research Laboratory, School of Physics and Astronomy, University of Birmingham, Birmingham B15 2TT, United Kindgom

[§]Teer Coatings Ltd., Berry Hill Industrial Estate, Droitwich, Worcestershire WR9 9AS, United Kindgom

Supporting Information

ABSTRACT: This report focuses on a novel strategy for the preparation of transition metal−MoS_2 hybrid nanoclusters based on a one-step, dual-target magnetron sputtering, and gas condensation process demonstrated for Ni-MoS_2. Aberration-corrected STEM images coupled with EDX analysis confirms the presence of Ni and MoS_2 in the hybrid nanoclusters (average diameter = 5.0 nm, Mo:S ratio = 1:1.8 ± 0.1). The Ni-MoS_2 nanoclusters display a 100 mV shift in the hydrogen evolution reaction (HER) onset potential and an almost 3-fold increase in exchange current density compared with the undoped MoS_2 nanoclusters, the latter effect in agreement with reported DFT calculations. This activity is only reached after air exposure of the Ni-MoS_2 hybrid nanoclusters, suggested by XPS measurements to originate from a Ni dopant atoms oxidation state conversion from metallic to 2+ characteristic of the NiO species active to the HER. Anodic stripping voltammetry (ASV) experiments on the Ni-MoS_2 hybrid nanoclusters confirm the presence of Ni-doped edge sites and reveal distinctive electrochemical features associated with both doped Mo-edge and doped S-edge sites which correlate with both their thermodynamic stability and relative abundance.

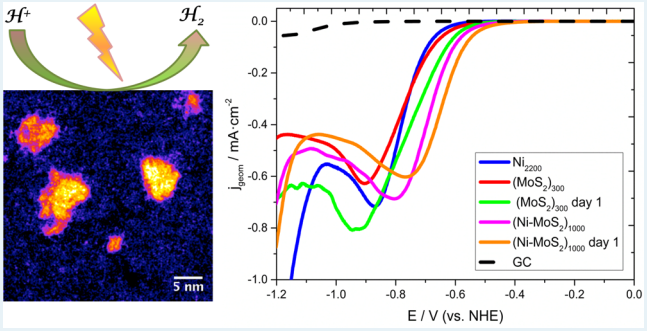

KEYWORDS: *molybdenum disulfide, nanoclusters, hydrogen evolution, doping, magnetron sputtering deposition, STEM*

INTRODUCTION

Transition metal dichalcogenides (TMDs) have emerged as promising materials for electrocatalytic applications. Initially used as hydrodesulfurisation catalysts, the discovery of the linear dependence of the electrochemically assisted hydrogen evolution reaction (HER) on the number of molybdenum disulfide (MoS_2) edge sites[1] has resulted in intensive research. In the case of MoS_2, the focus is on maximizing the proportion of active edge sites and minimizing the in-plane/through-plane charge transfer resistance by the development of single-layered nanoplatelets,[2] nanowires,[3] mesoporous structures,[4] and nanocomposites with highly conductive supports.[5] Only the Mo-edge sites are active to HER due to their near-zero hydrogen adsorption free energy (ΔG_H = 0.06 eV).[6]

Several methods have been proposed to enhance the HER activity, most of them concerning the sulfur enrichment of the Mo-edge sites.[7,8] A promising alternative is the doping of the S-edge sites to activate their HER activity.[9] DFT calculations have demonstrated that transition metal (TM) doping (Fe, Co, Ni) of the S-edge sites shifts the ΔG_H value closer to ΔG_H = 0 (thermo-neutral). The weakening of the S-doping metal bond on the MoS_2 edge strengthens the H−S binding on the S-edge up to an optimal level for catalyzing the HER.[10] Experiments on MoS_2 nanoparticles and MoS_3 thin films reported an HER enhancement upon nonselective edge doping,[11,12] and later tests on edge-terminated MoS_2 nanofilms correlated the 2-fold (in the case of Cu dopant) and almost 3-fold (for Fe, Co, Ni) HER enhancement observed with the activation of the S-edge sites.[13] Surprisingly, TM-doping on MoS_2 nanoparticles (NPs) is scarcely reported probably due to the difficulty in separating the effects of surface area and morphology changes from the electrocatalytic enhancement.[14,15]

Recently reported lamellar MoS_2 NPs, prepared by magnetron-sputtering and gas condensation to create nanoclusters in the gas phase prior to deposition, are excellent candidates for TM-doping due to their narrow size-distribution and the present ability to control the stoichiometry in the cluster beam source.[16] Previous investigations from our group demonstrated

Received: May 6, 2016
Revised: July 22, 2016
Published: August 2, 2016

DOI: 10.1021/acscatal.6b01274
ACS Catal. 2016, 6, 6008−6017

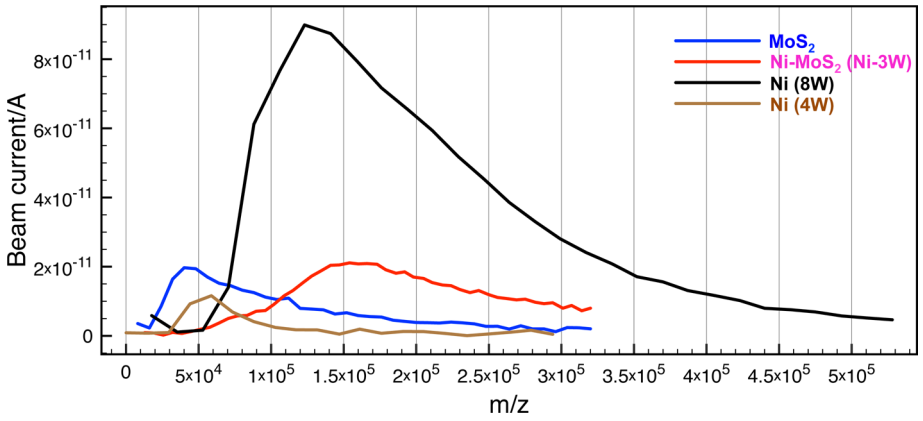

Figure 1. Mass spectra obtained by time-of-flight. From the spectra, MoS_2, Ni (8W), and Ni-MoS_2 (3W) show peak masses of around 4.8×10^4 amu ($(MoS_2)_{300}$), 1.3×10^5 amu (~Ni_{2200}), and 1.6×10^5 amu $\{(MoS_2)_{1000}\}$, respectively. The mass spectra of Ni (4W) is also plotted to show the effect of the power applied to this target.

that magnetron-sputtered MoS_2 nanoclusters are amorphous and S-deficient (Mo:S ratio = 1:1.6 ± 0.1).[16] Xu et al. report 2H-MoS_2 nanosheets fabricated by means of a gas-phase quartz furnace method that yields crystalline and S-enriched MoS_2 edges resulting in a significantly improved performance over naturally occurring MoS_2.[17] Pumera et al. observed a substantial increase in both HER overpotential and Tafel slope in chalcogen-deficient TMDs,[18] which can be ascribed in the case of MoS_2 nanoclusters to a deficiency of active sites and the formation of oxide species MoO_2/MoO_3 at the S-deficient sites unstable to cathodic potentials in acidic media.[3]

We report a novel methodology for preparing Ni-MoS_2 NPs via a one-step, dual-target, magnetron-sputtering, and gas condensation deposition technique. Pristine MoS_2 and Ni nanoclusters as well as Ni-MoS_2 hybrid nanoclusters are prepared to evaluate their electrocatalytic activity to HER. $(Ni\text{-}MoS_2)_{1000}$ hybrid nanoclusters exhibit an almost 3-fold increase in HER activity with respect to undoped $(MoS_2)_{300}$ nanoclusters, consistent with previous experimental studies on MoS_2 thin films.[13] Anodic stripping voltammetry (ASV) experiments on aged $(Ni\text{-}MoS_2)_{1000}$ hybrid nanoclusters reveal four distinctive electro-oxidative peaks, two of them correlated with the Ni-doped Mo-edge and S-edge sites by their abundance ratio and thermodynamic stability.

EXPERIMENTAL METHODS

Dual-Target Magnetron Sputtering Deposition of Ni, MoS_2, and Ni-MoS_2 Nanoclusters. MoS_2, Ni, and hybrid Ni-MoS_2 nanoclusters were prepared using a custom-built cluster beam source at Teer Coatings Ltd. (Worcestershire, U.K.). The system layout is shown in the Supporting Information (SI), Figure S1, and a more detailed description is available in the literature.[19]

During the cluster deposition, a condensation length (i.e., the distance between sputtering target surface and the exit nozzle) of 24 cm was used, and a pressure of approximately 0.23 mbar was maintained in the condensation chamber, with 70 standard cubic centimeters per minute (sccm) argon flow and 10 sccm helium flow. In the preparation of pure MoS_2 or Ni clusters, only the magnetron sputtering source fitted with the respective target (MoS_2 or Ni) was operated, whereas the other magnetron's power supply was switched off. For the deposition of Ni-doped MoS_2 clusters, the two magnetrons were operated simultaneously.

Physical Characterization of Ni, MoS_2, and Ni-MoS_2 Nanoclusters. Clusters were deposited on TEM grids covered with amorphous carbon films for scanning transmission electron microscopy (STEM) characterization. The clusters were imaged with a 200 kV aberration-corrected STEM (JEM 2100F) in the high-angle annular dark-field (HAADF) mode, and energy-dispersive X-ray spectroscopy (EDX) was also performed to analyze the elemental composition. X-ray photoelectron spectroscopy (XPS) was performed on a Kratos Axis His X-ray photoelectron spectrometer fitted with a charge neutralizer and magnetic focusing lense employing Mg Kα achromatic radiation (1253.6 eV). Spectral fitting was performed using CasaXPS version 2.3.15 with spectra energy-corrected to the adventitious C 1s peak at 284.6 eV.

Electrochemical Characterization. Electrochemical measurements were carried out in a thermostated three-electrode electrochemical cell (295 ± 2 K) with a PC-controlled PGSTAT128N potentiostat (Metrohm Autolab B.V, Netherlands). The electrodes used were a saturated calomel (SCE) reference electrode (BAS Inc., Japan), a bright Pt mesh counter electrode (Alfa Aesar Ltd., U.K.), and 5 mm diameter, 3 mm thick glassy carbon (GC) type 2 stubs (Alfa Aesar, U.K.) modified with either pure Ni or Ni-doped/undoped MoS_2 nanoclusters as working electrodes.

Prior to modification, GC stubs were polished to a mirror finish using decreasing size diamond (45 to 3 μm) and alumina slurries (1 to 0.05 μm) on a Buehler MetaServ 250 grinder-polisher using Trident/Microcloth polishing pads. The modified GC stubs were electrically connected to a brass rod embedded in Teflon (Direct Plastics Ltd., U.K.), insulating their lateral perimeter with epoxy resin to ensure that only the nanocluster-modified cross-section was exposed. All nanocluster-modified GC samples were transported to the electrochemical cell in a sealed container under N_2 atmosphere to avoid exposure to air.

All experiments were performed in a 2 mM $HClO_4$ (ACS ≥ 70%, Sigma-Aldrich), 0.1 M $NaClO_4$ (ACS ≥ 98%, Sigma-Aldrich) solution (pH 2.70), freshly prepared with ultrapure water (resistivity not less than 18.2 MΩcm, Millipore Milli-Q Direct 8). Deoxygenation was achieved by vigorous N_2 bubbling prior to each electrochemical experiment, and maintained under positive N_2 pressure. This electrolyte was chosen in contrast to other electrolytes more commonly reported in the literature for hydrogen evolution experiments

DOI: 10.1021/acscatal.6b01274
ACS Catal. 2016, 6, 6008−6017

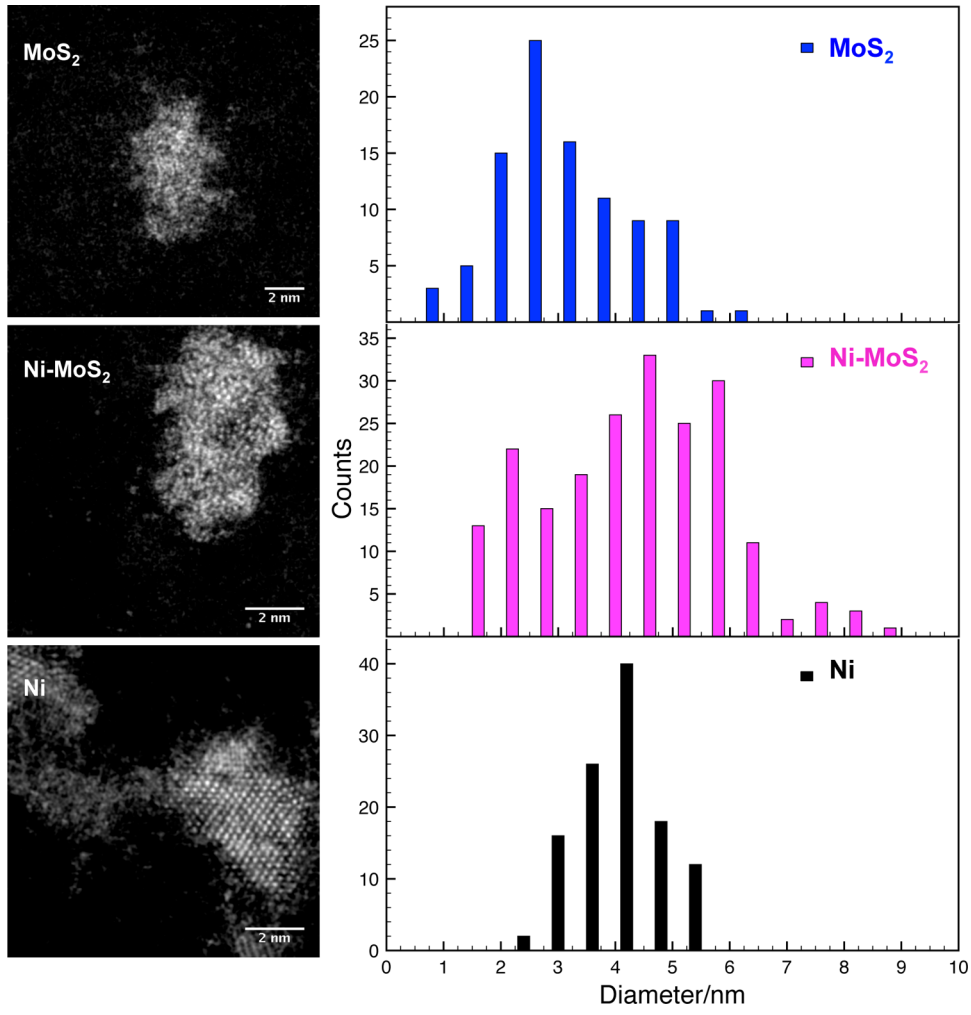

Figure 2. STEM images and size distribution in diameter based on the nanocluster surface area. MoS_2, Ni-MoS_2, and Ni (8W) have a peak value of 2.6, 5.0, and 4.2 nm, respectively.

(0.5 M H_2SO_4, pH ≈ 0.3; 0.1 M $HClO_4$, pH ≈ 1) due to the noncoordinating nature of the perchlorate anion being likely to yield more reproducible results and enable a more accurate elucidation of the reaction kinetic parameters. All experimental glassware was cleaned overnight by soaking in a dilute solution of $KMnO_4$ (ACS ≥ 99%, Sigma-Aldrich) in concentrated H_2SO_4 (>95% analytical grade, Fisher Scientific), followed by thorough rinsing with ultrapure water.

The modified electrodes were preconditioned with 10 cycles between −0.045 and −1.645 V vs SCE at a scan rate of 50 mVs^{-1}. Electrocatalytic measurements were made at a range of voltage scan rates from 2 to 1200 mVs^{-1}. This experimental procedure was applied to both freshly deposited and 14-h air-exposed samples. An estimation of the surface coverage for $(MoS_2)_{300}$, Ni_{2200}, and $(Ni\text{-}MoS_2)_{1000}$ was obtained with the hydrogen evolution experiments by performing the least-squares linear regression of the HER peak current intensity ($|I_{P,HER}|$) vs the square root of the scan rate ($v^{1/2}$) to fit the Randles−Sevčik expression for irreversible redox processes (SI, Figure S5 and Table S1).

ASV experiments, consisting of 10 cycles in the 0 to 1.2 V voltage range versus SCE, were performed on both of the 14-h air-exposed electrochemically tested MoS_2 and Ni-doped MoS_2 samples to estimate their turnover frequency and elucidate their electrochemical features. All voltammograms were later plotted with respect to the normal hydrogen electrode (NHE).

RESULTS AND DISCUSSION

Analysis of Magnetron Sputtering Deposited Ni, MoS_2, and Hybrid Ni-MoS_2 Nanoclusters. The time-of-flight mass filter enabled the mass of nanoclusters formed to be monitored before deposition onto the GC stubs. Figure 1 shows the mass spectra of the samples employed in the HER measurements. During the preparation of pure MoS_2 samples, a sputtering power of 8W was applied to the MoS_2 target and a peak mass of 4.8×10^4 amu, equivalent to $(MoS_2)_{300}$, was found in the mass spectra (300 being the number of MoS_2 units contained in one MoS_2 nanocluster). The pure Ni sample was prepared similarly, and a resulting Ni peak mass of 1.3×10^5 amu, equivalent to ~ Ni_{2200}, was found (2200 being the number of Ni atoms in one Ni nanocluster). When the sputtering power for the Ni target was changed from 4W to 8W, the peak mass shifted from 6×10^4 amu to 1.3×10^5 amu, and the peak beam current shifted from 11 pA to 90 pA. Thus, higher sputtering power on the Ni target generates more, and larger, Ni nanoclusters. Consequently, a lower sputtering power of only 3W on the Ni target was used in the preparation of the hybrid Ni-MoS_2 nanoclusters in order to avoid an excess of Ni nanoclusters, whereas 8W of sputtering power was used on the

DOI: 10.1021/acscatal.6b01274
ACS Catal. 2016, 6, 6008−6017

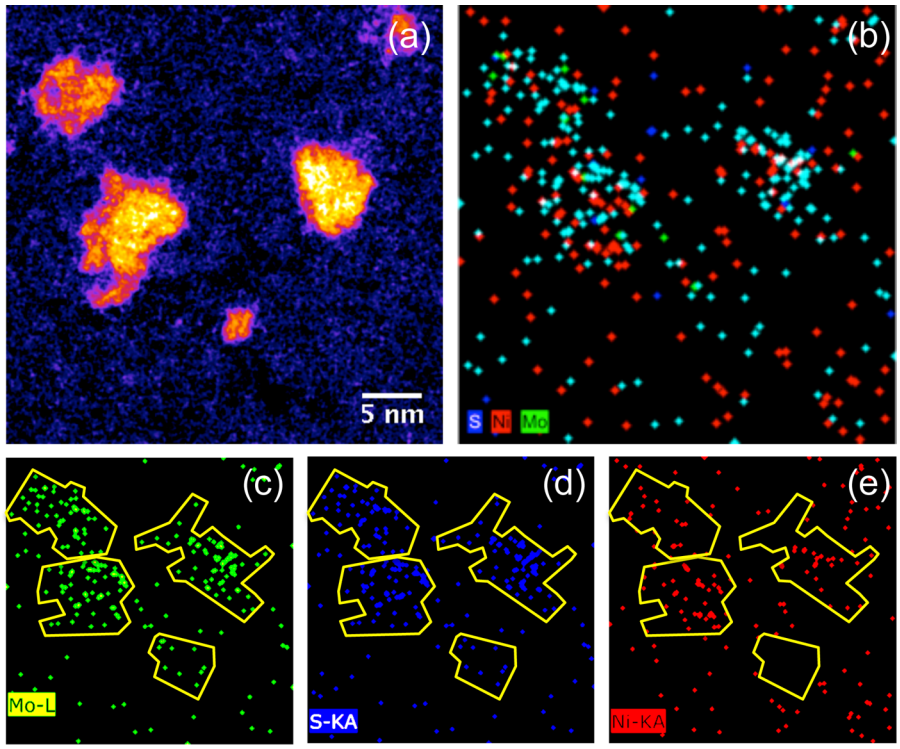

Figure 3. STEM image (a) containing large and small nanoclusters used for EDX measurement. (b) EDX mapping shows the composition of Ni-MoS_2 nanoclusters; Mo, S, and Ni are shown in green, blue, and red, respectively. Signal in cyan comes from the overlap of Mo and S signals. Mo, S, and Ni signals are also shown separately in pannels c, d, and e, where the nanocluster positions are marked by the yellow shapes.

MoS_2 target. The peak mass of the hybrid Ni-MoS_2 nanoclusters was located at 1.6×10^5 amu, equivalent to a mass of $(MoS_2)_{1000}$ (1000 equiv MoS_2 units per Ni-MoS_2 nanocluster) or Ni_{2712} (2712 equiv Ni atoms per Ni-MoS_2 nanocluster). In the following sections, we will refer to the Ni, MoS_2, and hybrid Ni-MoS_2 nanoclusters as Ni_{2200}, $(MoS_2)_{300}$, and $(Ni\text{-}MoS_2)_{1000}$, respectively.

The STEM images in Figure 2 show (top to bottom) the morphologies of MoS_2 nanoclusters, Ni-MoS_2 hybrid nanoclusters, and Ni nanoclusters. An HAADF-STEM image is a Z-contrast image, meaning that the image intensity depends on the atomic number of elements,[20] and in practice, the images are dominated by Mo atoms. The distinct intensity contrast across one MoS_2 nanocluster indicates an incomplete multilayer structure (the HAADF-STEM intensity line profile analysis is shown in Figure S2 SI). Ni-MoS_2 nanoclusters present a broadly similar morphology to that of the pure MoS_2 nanoclusters, whereas Ni nanoclusters show a quite distinct crystalline structure. This implies that Ni is atomically added to the MoS_2 nanoclusters when the hybrid Ni-MoS_2 nanoclusters are formed. After FFT analysis of STEM images in Figure 2 and S2 (SI) and comparison with the crystalline lattice parameters of MoS_2 polymorphs 1T and 2H, no clear crystalline structure could be found on either MoS_2 or Ni-MoS_2 nanoclusters. Based on the projected surface areas of tens of nanoclusters of each kind, the average diameter distributions are shown in Figure 2. The peak values in the distributions for MoS_2 nanoclusters, Ni-MoS_2 nanoclusters, and Ni nanoclusters are 2.6, 5.0, and 4.2 nm, respectively.

In order to confirm the existence of Ni in the hybrid Ni-MoS_2 nanoclusters, EDX analysis was conducted, and the result is shown in Figure 3. Mo, S, and Ni signals are found in the same clusters, which indicate Ni-MoS_2 hybrid nanoclusters were made successfully. The characteristic energy difference between the Mo L-edge and S L-edge is only 14 eV, which is smaller than the energy resolution of the EDX instrument (133 eV). Consequently, Mo and S signals cannot be distinguished by EDX, and the cyan dots in Figure 3b are due to the signal overlap of Mo and S. Ni signals are found both in MoS_2 areas and between them, which means Ni might locate on or between MoS_2 nanoclusters. Figure 3c–e display the individual elemental maps. Nanocluster shape mismatch between HAADF-STEM images shown in Figure 3a and Figures 3b–e is ascribed to STEM image drift during EDX measurement. Compared with the large nanoclusters, the small nanocluster located at the bottom of each image is much less abundant in Ni, which is found primarily at MoS_2 edge sites and between nanoclusters. Besides the signals found in the nanoclusters (marked by the yellow shapes), signals can be found outside the nanoclusters; these signals may come from small clusters originating from the deposition process or electron beam sputtering of the deposited nanoclusters. Because Mo and S signals are overlapped with each other, the exact nanocluster compositions cannot be obtained from EDX analysis. To identify the composition of the hybrid Ni-MoS_2 nanoclusters, we employ a method based on atom counting and STEM intensity measurement (SI). By this method, the compositions of six nanoclusters of varying size were calculated and are listed in Table 1.The outcome is that there is no fixed ratio of Ni atoms to MoS_2 units in the hybrid nanoclusters, but in general, the proportion of Ni increases with nanocluster size, which agrees with the EDX results.

The chemical composition and oxidation state of the untested nanoclusters deposited on TEM grids analyzed by STEM imaging were further characterized by XPS. High-resolution spectra in the Mo 3d and S 2p region for fresh and

DOI: 10.1021/acscatal.6b01274
ACS Catal. 2016, 6, 6008–6017

Table 1. Composition Analysis of Six Hybrid Ni-MoS_2 Nanoclusters Based on HAADF-STEM Images

Ni-MoS_2 cluster	ratio of Ni atoms number to MoS_2 units number
$(MoS_2)_{373}Ni_{22}$	0.06
$(MoS_2)_{378}Ni_{30}$	0.08
$(MoS_2)_{461}Ni_{720}$	1.56
$(MoS_2)_{844}Ni_{648}$	0.77
$(MoS_2)_{1163}Ni_{1235}$	1.06
$(MoS_2)_{1458}Ni_{2181}$	1.50

14-h air-exposed $(Ni\text{-}MoS_2)_{1000}$ are shown in Figure 4. The fresh Mo 3d XPS spectrum can be deconvoluted into four components after the inclusion of the photoemission current characteristic of the carbon tape used to immobilized the TEM grids: one Mo $3d_{5/2}$ and Mo $3d_{3/2}$ spin−orbit doublet found at ∼229.8 eV and ∼232.9 eV with binding energies consistent with the binding energies found for the $(MoS_2)_{300}$ nanoclusters (Figure S3 SI) and characteristic of the Mo^{4+} oxidation state found in MoS_2 materials,[21] and an additional doublet at ∼233.1 eV and ∼236.2 eV related to the Mo^{6+} oxidation state found in MoO_3.[22] An upward shift of 0.2 eV in the Mo^{4+} and Mo^{6+} components after air exposure (for MoS_2 nanoclusters ∼0.4 eV, see Figure S3 SI) as well as a photoemission intensity increase of the latter doublet indicate an oxidation state increase in both MoS_2 and Ni-MoS_2 nanoclusters. This is supported by analysis of the Mo^{4+}:Mo^{6+} XPS atomic photoemission percentages (at. %), which reveal a conversion of MoS_2 into MoO_3 from Ni-MoS_2 fresh samples (Mo^{4+}/Mo^{6+} 78.1/21.9 at. %) to air exposed (Mo^{4+}/Mo^{6+} 54.9/45.1 at. %). The fresh S 2p spectrum can be deconvoluted into two components at ∼160.7 eV and ∼161.9 eV, corresponding to the spin−orbit S $2p_{3/2}$:$2p_{1/2}$ doublet characteristic of the S^{2-} oxidation state,[23] and we observe that an additional broad signal at ∼167 eV related to oxidized sulfur species such as sulfites or sulfates[24] is also found on $(MoS_2)_{300}$ nanoclusters (Figure S3 SI). Quantification of the Mo^{4+}:S^{2-} peak areas confirmed the S-deficient nature of $(MoS_2)_{300}$ nanoclusters (1:0.90 ± 0.02), while $(Ni\text{-}MoS_2)_{1000}$ nanoclusters present a 1:1.8 ± 0.1 ratio similar to the Mo:S ratio expected in MoS_2 (1:2). Such difference in the oxidation behavior could be ascribed to the presence of surface Ni atoms prone to oxidation, which would mitigate S^{2-} oxidation under ambient conditions. The lack of definition in the spin−orbit S $2p_{3/2}$:$2p_{1/2}$ doublet found here had been previously ascribed in amorphous MoS_3 materials to the presence of mixed S^{2-}/S_2^{2-} oxidation states,[25] but in our case, it could be due either to the low photoemission counts due to low sample loading (∼4 μg cm^{-2}) or to the inherent amorphous nature of the MoS_2 nanoclusters provided the S-deficiency of the samples.

Analysis of the Ni 2p high-resolution spectra of both Ni and Ni-MoS_2 nanoclusters is paramount to evaluate the oxidation state of the Ni dopant atoms as well as to identify the presence of nickel species such as oxides and sulfides. Deconvolution of the Ni $2p_{3/2}$ component of the untested Ni nanoclusters (Figure S4 SI) shows the predominance of oxidized species such as NiO and $Ni(OH)_2$, with Ni:NiO:$Ni(OH)_2$ composition percentages practically invariable after air exposure (7.4:49.8:42.8 fresh, 6.6:51.2:42.2 air exposed). As for $(Ni\text{-}MoS_2)_{1000}$ nanoclusters (Figure 5), quantitative analysis of the Ni 2p region is not possible due to low signal-noise ratio ascribed to the low Ni content aimed during the nanocluster formation. The peak position of the Ni $2p_{3/2}$ component for the fresh $(Ni\text{-}MoS_2)_{1000}$ samples at ∼852.8 eV and the lack of clearly defined satellite signals seem to suggest predominance of metallic Ni (theoretical value: 852.7 ± 0.4 eV),[26] but air exposure leads to an upward shift of the Ni $2p_{3/2}$ component to ∼854 eV, similar to the 854.6 eV characteristic of the NiO principal XPS peak[27] as well as in increase in the Ni $2p_{3/2}$ and Ni $2p_{1/2}$ satellite intensities (∼861 and ∼872.5 eV, respectively). This would indicate that under air exposure the doping Ni atoms spontaneously increase their oxidation state to Ni^{2+} as found in NiO species, agreeing with the behavior observed for bare Ni nanoclusters. Presence of a nickel sulfide phase cannot be discarded from XPS results as it is well reported that directly bonded S atoms leave the Ni $2p_{3/2}$ peak position unaltered,[28] and the S $2p_{3/2}$:$2p_{1/2}$ doublet overlap commonly reported in nickel sulfides[29] is also found in the bare $(MoS_2)_{300}$ nanoclusters. However, the upward shift of the Ni $2p_{3/2}$ component to binding energies similar to those of NiO species after air exposure makes the presence of a nickel sulfide phase unlikely. Thus, the Ni oxidation state conversion observed after 14 h air exposure will have significant repercussions in the electrocatalytic performance of the Ni-MoS_2 hybrid nanoclusters.

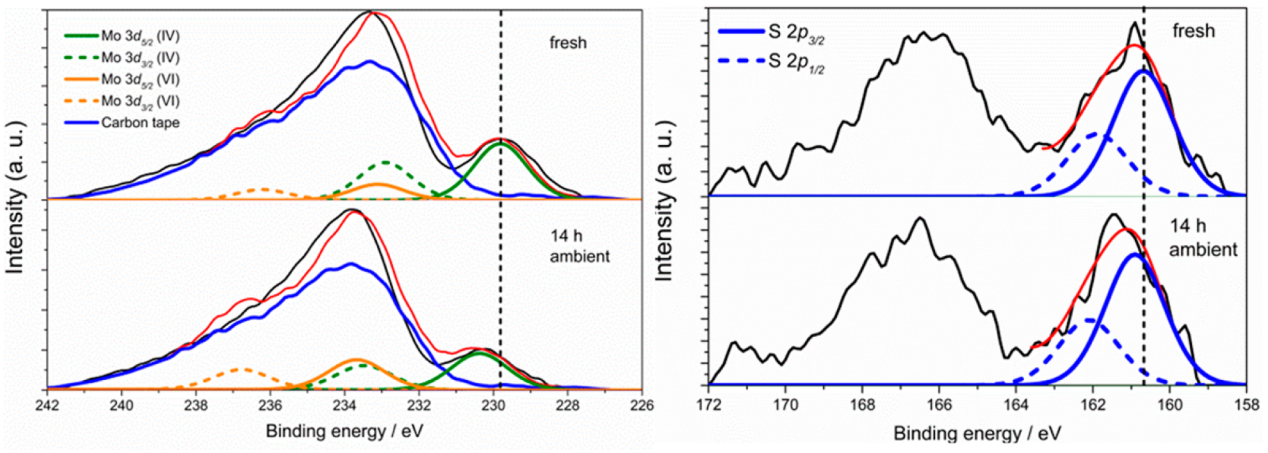

Figure 4. High-resolution XPS spectra of Mo 3d (left) and S 2p (right) for fresh (top) and 14-h air-exposed (bottom) $(Ni\text{-}MoS_2)_{1000}$ nanoclusters. Labels: raw spectra (solid black), cumulative peak fit (solid red), Mo^{4+} $3d_{5/2}$ (solid green), Mo^{4+} $3d_{3/2}$ (dashed green), Mo^{6+} $3d_{5/2}$ (solid orange), Mo^{6+} $3d_{3/2}$ (dashed orange), S $2p_{3/2}$ (solid blue) and S $2p_{1/2}$ (dashed blue).

DOI: 10.1021/acscatal.6b01274
ACS Catal. 2016, 6, 6008−6017

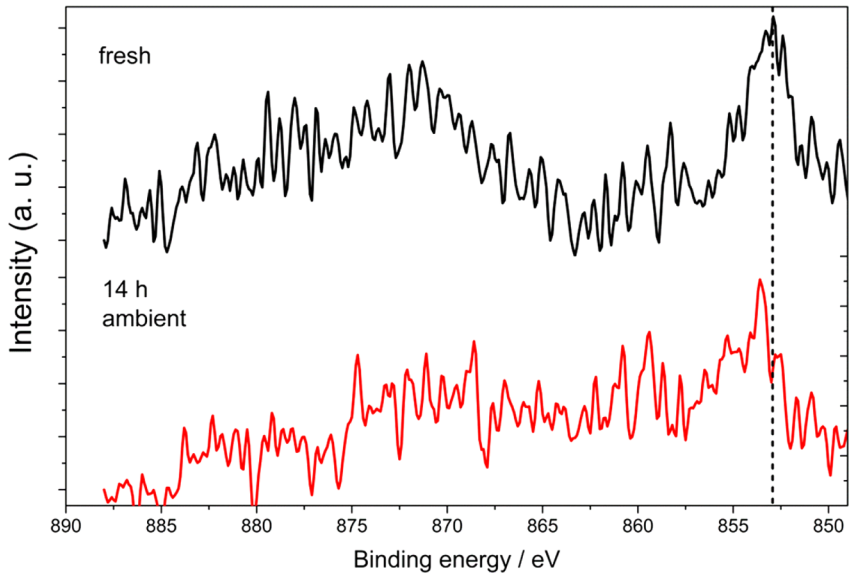

Figure 5. High-resolution XPS spectra of Ni 2p for fresh (top, solid black) and 14-h air-exposed (bottom, solid red) $(Ni\text{-}MoS_2)_{1000}$ nanoclusters. Dashed vertical line indicates peak position of metallic Ni (theoretical value: 852.7 ± 0.4 eV).[26]

Evaluation of Electrocatalytic Activity to Hydrogen Evolution Reaction (HER). Figure 6 shows the linear sweep voltammograms acquired in the 0 to −1.2 V range (normalized vs NHE) at a scan rate of 25 mVs^{-1} in 2 mM $HClO_4$/0.1 M $NaClO_4$ aqueous electrolyte for all samples tested. A diffusion decay peak profile is observed in all samples due to the low proton concentration present in the electrolyte ($[H^+] \approx 2 \times 10^{-6}$ mol cm^{-3}), purposefully chosen to perform a better elucidation of the samples' kinetic parameters and surface coverage (Tafel slope analysis and irreversible Randles−Sevčik equation, see SI for the latter).

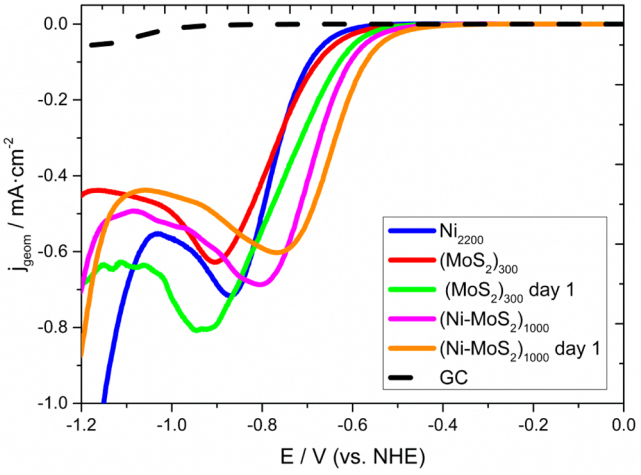

Figure 6. Linear sweep voltammograms recorded at 5 mm diameter glassy carbon (dashed black) samples modified with (a) fresh $(MoS_2)_{300}$ (solid red), (b) fresh $(Ni\text{-}MoS_2)_{1000}$ (solid magenta), (c) Ni_{2200} (solid blue), (d) 14-h air-exposed $(MoS_2)_{300}$ (solid green), and (e) 14-h air-exposed $(Ni\text{-}MoS_2)_{1000}$ (solid orange) nanoclusters in the 0 to −1.2 V range vs NHE. Scan rate: 25 mV s^{-1}.

Freshly prepared $(MoS_2)_{300}$ nanoclusters (Figure 6a) exhibit an onset potential of ca. 650 mV, reaching a peak half-maximum current density ($j_{half\ max}$) of 0.31 mA cm^{-2} at an overpotential (η) of ca. 770 mV. The experimental onset potential is approximately 400 mV higher than that of 2H-MoS_2 nanosheets reported in the literature (ca. 200 mV vs NHE):[1,11,30] this originates from the MoS_2 preparation methodology and hence the degree of sulfur enrichement.

The main factors that hinder HER activity in MoS_2 materials are their intrinsic conductivity, metal-to-chalcogen ratio, edge site abundance, and catalyst loading. Previous investigations from our research group demonstrated that magnetron-sputtered MoS_2 size-selected nanoclusters presented a 2-layer thickness in the 150−500 unit range.[16] This issue has again been observed in this investigation, where $(MoS_2)_{300}$ nanoclusters exhibit an incomplete multilayered structure ranging from 1 to 4 layers (see Figure S2 SI). As through-plane electron mobility in MoS_2 is 2200 times slower than in-plane,[31] the absence of single-layered clusters hampers the electrocatalytic activity. XPS analysis performed in this study have revealed that both $(MoS_2)_{300}$ and $(Ni\text{-}MoS_2)_{1000}$ nanoclusters are S-deficient. A high correlation between metal-to-chalcogen ratio and HER activity has been extensively reported. Eng et al. observed a substantial increase in both HER overpotential and Tafel slope in chalcogen-deficient TMDs,[18] which can be ascribed in the case of MoS_2 to a deficiency of active sites and the formation of oxide species MoO_2/MoO_3 at the S-deficient sites unstable to cathodic potentials in acidic media,[3] experimentally confirmed by XPS measurements reported here.

Sulfur-rich MoS_2 nanostructures with enhanced HER activities and stability in acidic environment have been prepared by use of gas-phase[4] or liquid-phase[32] methods. However, evidence has shown that the morphology of MoS_2 is modified by the exposure and composition of the sulfur gas phase[33,34] or liquid phase.[32] Thus, ex-situ sulfidation treatments were not performed to guarantee that the HER enhancement in the samples is unambiguously due to the Ni-doping of the edge sites. In addition to this, reports by Vrubel et al. and Rowley-Neil et al. revealed that the HER activity of the molybdenum sulfide catalysts is correlated with the catalyst loading: higher molybdenum sulfide catalyst loading lead to enhanced HER performance.[35,36] Thus, the HER performance of our nanoclusters cannot be unambiguously judged by the current density values obtained at the same overpotentials as those reported by

DOI: 10.1021/acscatal.6b01274
ACS Catal. 2016, 6, 6008−6017

the literature. Assuming a cluster interspacing of 2.5 nm, the mass loadings for Ni_{2200}, $(MoS_2)_{300}$ and $(Ni\text{-}MoS_2)_{1000}$ are 1.28, 3.45, and 4.25 $\mu g\ cm^{-2}$, respectively. These values are at least 1 order of magnitude smaller than those reported in more competitive MoS_2 materials,[4,37] supporting our claims that the low catalyst loadings lead to overpotentials higher than those reported in the literature.

Electrochemical testing of the $(MoS_2)_{300}$ nanoclusters after the aforementioned testing and exposure to air for 14 h indicates an enhancement in their electrocatalytic performance to the HER, with a $j_{half\ max}$ of ca. 0.40 mA cm^{-2} at $\eta \approx 749$ mV. This is due to the dissolution of the $(MoS_2)_{300}$ nanoclusters outermost layers due to the conversion of MoS_2 to MoO_3, a compound soluble in acidic conditions. Yu et al. observed that electrochemical cycling of bilayered MoS_2 nanoflakes assisted in the oxidation of Mo^{4+} to Mo^{6+} ascribed to air exposure, leading to the complete loss of the MoS_2 outermost layer after reimmersion in the acidic electrolyte used. The loss of such layer resulted in enhanced HER performance and Tafel slope, concluding that the loss of a full MoS_2 monolayer increases the HER activity by a factor of ~4.47.[38,39,40,41] As the $(MoS_2)_{300}$ nanoclusters have been shown to consist of an incomplete multilayered structure (1 to 4 MoS_2 layers thick, see Figure S2 SI), any loss of the outermost layers will consequently enhance the HER activity.

Analogous voltammograms were recorded for $(Ni\text{-}MoS_2)_{1000}$ hybrid nanoclusters (Figure 6b). It can be seen that $(Ni\text{-}MoS_2)_{1000}$ hybrid nanoclusters exhibit a significant improvement in the electrocatalytic activity with respect to the undoped counterparts: the onset potential is reduced by ca. 100 mV and the $j_{half\ max}$ (0.35 mA cm^{-2}) is reached at $\eta \approx 680$ mV (100 mV less than $(MoS_2)_{300}$ nanoclusters). To confirm that the HER enhancement is due to the effective Ni-doping of the S-edge sites and not to the presence of HER-active Ni nanoclusters in the sample, the response of a GC sample modified with Ni nanoclusters (average atomic mass units= 2200, Figure 6c) was evaluated. Ni_{2200} nanoclusters exhibited an onset potential and $j_{half\ max}$ similar to $(MoS_2)_{300}$ nanoclusters (0.36 mA cm^{-2}, $\eta \approx$ 770 mV) but with faster HER kinetics (as per Tafel analysis, vide infra). This is evidenced by the fact that Ni_{2200} nanoclusters achieve a peak current density (j_p) of 0.72 mA cm^{-2} at $\eta \approx 870$ mV whereas $(MoS_2)_{300}$ nanoclusters only a j_p = 0.63 mA cm^{-2} at $\eta \approx 905$ mV. Thus, we can satisfactorily conclude that the HER enhancement observed in $(Ni\text{-}MoS_2)_{1000}$ nanoclusters is due to the increase in active edge sites density upon Ni-doping of the initially inactive S-edge sites.

Combined analysis of exchange current density (j_0) and turnover frequency (TOF) values provides insight on the predicted HER enhancement by Ni-doping as well as an indication of the intrinsic activity per-site.[9] Freshly prepared $(MoS_2)_{300}$ and $(Ni\text{-}MoS_2)_{1000}$ nanoclusters presented similar j_0 values ($\approx 8 \times 10^{-10}$ A cm^{-2}), but after the above electrochemical experiments and 14-h air exposure $(Ni\text{-}MoS_2)_{1000}$ hybrid nanoclusters (Figure 6e) showed an almost 3-fold increase with respect to their initial j_0 value (2.1×10^{-9} vs 7.6×10^{-10}). This significant HER enhancement is in good agreement with previous reports that indicated a 3-fold increase in active sites but a worse per-site activity due to the overall less thermo-neutral ΔG_H values.[13] TOF values of the 14-h air-exposed samples support these conclusions: $(Ni\text{-}MoS_2)_{1000}$ nanoclusters exhibit a lower TOF value (60.3 $H_2\ s^{-1}$) than $(MoS_2)_{300}$ nanoclusters (67.1 $H_2\ s^{-1}$) at equivalent overpotentials (calculation performed at $(MoS_2)_{300}$ overpotential at $j_{half\ max}$), indicating an inferior per-site activity of the doped MoS_2 nanoclusters despite the increase in the density of edge sites. If TOF is calculated for $(Ni\text{-}MoS_2)_{1000}$ nanoclusters at their $j_{half\ max}$ overpotential, we obtain a value of 30.9 $H_2\ s^{-1}$. All results are summarized in Table S2 (SI).

Tafel slope analysis was then carried out to provide insight on the HER efficiency of the catalysts and on the HER reaction mechanism. Noble metals such as Pt follow the Volmer–Tafel mechanism, in which the rate-determining step is the chemical hydrogen desorption from the catalyst surface, with Tafel slopes $b \approx 30$ mV dec^{-1}.[24] Tafel slope analysis of the 25 mV s^{-1} cathodic scans (Figure 7) revealed that all the MoS_2 samples

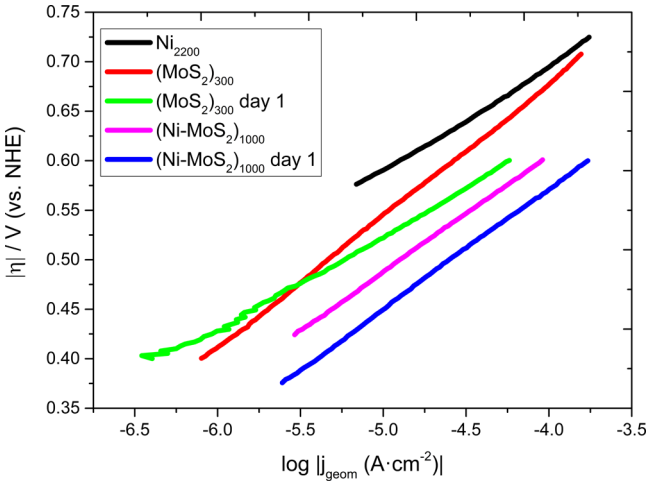

Figure 7. Tafel plots (η vs $\log|j_{geom}|$) of the Ni-doped/undoped MoS_2 nanoclusters evaluated in Figure 6. Scan rate: 25 mV s^{-1}.

are in the 95–130 mV dec^{-1} range, $(MoS_2)_{300}$ exhibiting the lowest Tafel slope (94 mV dec^{-1}) after exposure to air for 14 h. This compares to exfoliated MoS_2 layers reported to display Tafel slopes, $b \approx 120$ mV dec^{-1}, in agreement with the Volmer mechanism which dictates the monatomic hydrogen adsorption to be the limiting step.[25] Edge-rich nanosheets[26] and pure 1T-phase MoS_2[2] samples exhibited, respectively, $b \approx$ 55–60 mV dec^{-1} and $b \approx 40$ mV dec^{-1}.

Electrodissolution of oxygen-rich HER inactive regions or electrochemical exfoliation of MoS_2 outermost layers, previously reported in the literature, might expose edge-abundant nanocluster regions with higher through-plane conductivity that could explain $(MoS_2)_{300}$ lower Tafel slope after air exposure.[27] Ni_{2200} samples present a Tafel slope of 106 mV dec^{-1}, similar to the $b \approx 120$ mV dec^{-1} reported in the literature for electrodeposited Ni thin films.[28] When as-prepared Ni-doped/undoped MoS_2 nanoclusters are compared, Ni-doping does not decrease the Tafel slope value significantly, leaving the HER mechanism unchanged as reported previously.[13]

The HER enhancement of $(Ni\text{-}MoS_2)_{1000}$ hybrid nanoclusters after 14 h air exposure is probably related to the Ni surface: reports suggest this could comprise a spontaneously formed $NiO+Ni(OH)_2$ shell several atomic layers thick.[42] Oxygen present in the $NiO+Ni(OH)_2$ shell acts a proton-acceptor site, reported both theoretically and experimentally to catalyze HER.[43,44] The presence of NiO after 14 h air exposure of $(Ni\text{-}MoS_2)_{1000}$ hybrid nanoclusters has been confirmed by XPS measurements (see previous analysis), which is also expected to be found in the samples tested electrochemically.

DOI: 10.1021/acscatal.6b01274
ACS Catal. 2016, 6, 6008–6017

This effect would synergistically contribute to the HER enhancement already observed for 14-h air-exposed $(MoS_2)_{300}$ related to dissolution of the MoS_2 outermost layers.

Electrochemical Features of MoS_2 and Ni-MoS_2 Hybrid Nanoclusters: Anodic Stripping Voltammetry. Anodic stripping voltammetry (ASV) experiments were performed on the 14-h air-exposed samples to estimate numerically their turnover frequency (see SI) and elucidate their electrochemical features. Figure 8a shows the voltammo-

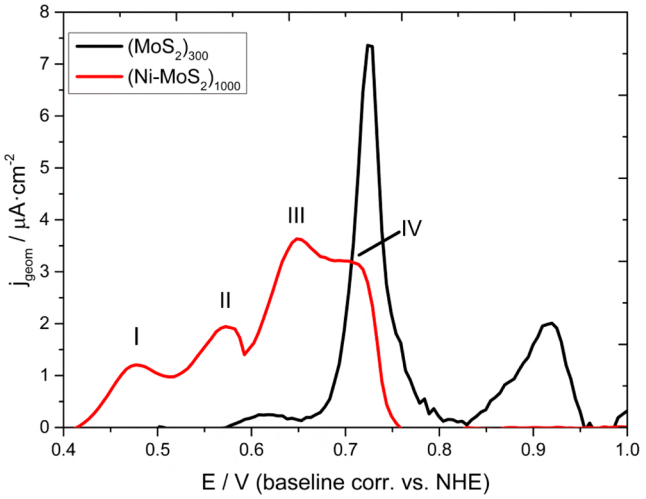

Figure 8. Anodic stripping voltammograms of 14-h air-exposed (a) $(MoS_2)_{300}$ nanoclusters (solid black) and (b) $(Ni\text{-}MoS_2)_{1000}$ hybrid nanoclusters (solid red) deposited on a 5 mm glassy carbon stub in the 0.5 to 1 V range versus NHE. Scan rate: 50 mV s^{-1}.

grams obtained for $(MoS_2)_{300}$ nanocluster-modified GC electrode. The two oxidation peaks at ca. 0.72 and 0.92 V versus NHE these correspond to the selective oxidation of the MoS_2 edge-plane sites (Mo- edges) and basal-plane sites, respectively,[11] by the irreversible oxidation of Mo metal centers from oxidation state +4 to +6.[25] The metastable edge sites require lower overpotentials to drive their oxidation, whereas the thermodynamically favored basal-plane sites necessitate higher overpotentials for their electrochemical oxidation.[45]

Next, analogous experiments were conducted on the $(Ni\text{-}MoS_2)_{1000}$ hybrid nanoclusters-modified GC electrode, with the results given in Figure 8b. In contrast to the undoped MoS_2 nanoclusters, the ASV presents a broad signal in the 0.4 to 0.8 V region on the first anodic sweep, which is no longer present in further scans. Deconvolution of the voltammetric profile reveals that the signal consists of four oxidation peaks at ca. 0.48 V (peak I), 0.57 V (peak II), 0.65 V (peak III), and 0.72 V (peak IV), respectively (for unconstrained peak deconvolution see Figure S6 SI). The peak IV potential is in agreement to the oxidation of undoped edge-plane sites experimentally observed in $(MoS_2)_{300}$ nanoclusters.

The absence of any other electrochemical features from bare MoS_2 implies that the remaining anodic peaks are necessarily related to oxidation processes at either bare Ni or Ni-doped MoS_2 sites. Analysis of the Ni electro-oxidation reaction mechanism in acidic media (SI) allows us to ascribe peak I to the formation of the $Ni(OH)_2$ anodic layer originated from Ni nanoclusters/atoms not located at MoS_2 active edge sites (i.e., in MoS_2 basal planes or in direct contact with the GC electrode). Coverage of the basal-plane sites by Ni atoms/aggregates is suspected to mask the inherent electrochemical activity of the MoS_2 basal planes, of which their electro-oxidative activity is absent in the $(Ni\text{-}MoS_2)_{1000}$ ASV. Further analysis of the integrated charge density $\langle\sigma_q\rangle$ of the ASV peaks supports this claim, as the $\langle\sigma_q\rangle$ value for peak I observed in the $(Ni\text{-}MoS_2)_{1000}$ hybrid nanoclusters ASV (approximately 9.7 μC cm^{-2}) is almost equivalent to that observed for the $(MoS_2)_{300}$ nanoclusters basal-plane ASV ($\langle\sigma_q\rangle$ approximately 14.4 μC cm^{-2}), indicating an almost entire coverage of the MoS_2 basal plane sites by Ni.

Ni doping, according to recent DFT calculations of ΔG_H values in MoS_2 nanoclusters[13] and experimental reports, could effectively dope both the already-active Mo-edge sites and the initially inactive S-edge sites.[15,46] This results in two active sites per two MoS_2 units at the S-edge and one active site per two MoS_2 units at the Mo-edge with a theoretical Mo-edge:S-edge abundance ratio of 1:2. Activation of the thermodynamically favored basal planes would have significant implications in the enhancement of the electrocatalytic activity of TMDs, as all their surface would be active to the HER. Recent reports have successfully achieved the activation of the basal planes by incorporation of platinum in the in-plane structure[47] or the formation of strained sulfur vacancies in 2H-MoS_2.[48] However, the possibility of Ni doping of the basal planes, although briefly mentioned by Wang et al. as one of the main challenges in transition metal doping,[13] was not considered in this study as no theoretical or experimental reports provide evidence of MoS_2 basal-plane activation after incorporation of transition metals above the basal-plane surface.

Assuming a correlation between the Mo-edge:S-edge natural abundance and electro-oxidative activity ratios, we should expect, if the Ni-doped sites have distinctive electro-oxidative features with respect to pristine active sites, that unidentified peaks II and III satisfy a 1:2 anodic peak ratio. Peak deconvolution of the anodic stripping voltammogram, upon application of a 1:2 peak II/peak III area ratio constraint, provides a satisfactory fit with $R^2 \approx 0.990$ (Figure 9). We therefore conclude that peaks II and III correspond to the

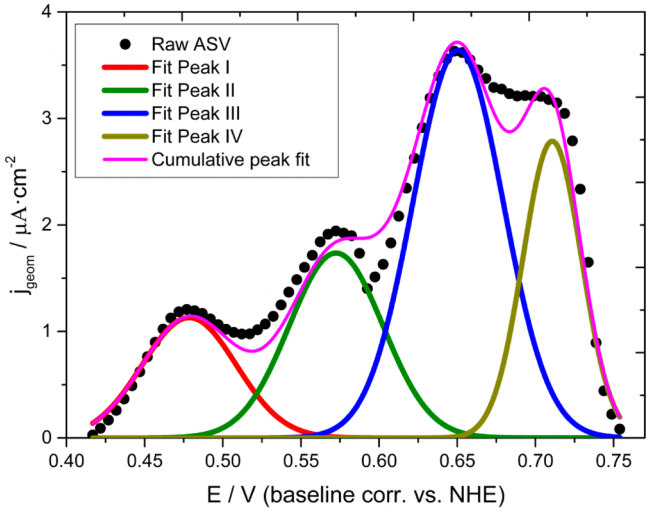

Figure 9. Peak deconvolution of the anodic stripping voltammogram (ASV) first scan of 14-h air-exposed $(Ni\text{-}MoS_2)_{1000}$ hybrid nanoclusters deposited on a 5 mm glassy carbon stub in the 0.4 to 0.8 V range vs NHE. Raw ASV (•) is deconvoluted in peaks I (solid red), II (solid green), III (solid blue), and IV (solid brown).

DOI: 10.1021/acscatal.6b01274
ACS Catal. 2016, 6, 6008−6017

electro-oxidation of doped Mo-edge and S-edge sites, respectively. To the best of our knowledge, this is the first time that site-dependent electrochemical features have been observed on TM-doped MoS_2 materials.

The large difference in the undoped edge plane sites peak intensity between the $(MoS_2)_{300}$ and the $(Ni\text{-}MoS_2)_{1000}$ hybrid nanoclusters can be understood by analysis of the integrated charge density of the electro-oxidative peaks found in the ASV. We would expect that, due to the fact that Ni doping does not occur selectively on the edge sites, some Mo-edge sites remain undoped. As a consequence, the sum of the ASV response of the Ni doped and Ni undoped Mo-edge sites in $(Ni\text{-}MoS_2)_{1000}$ nanoclusters should be (assuming equivalent catalyst loading and surface coverage) equivalent to the ASV response of the undoped Mo-edge sites present in $(MoS_2)_{300}$ nanoclusters.

The integrated charge density of the ASV peak at 0.72 V versus NHE observed in $(MoS_2)_{300}$ ascribed to the Mo-edge sites ($\langle\sigma_q\rangle$ approximately 32.7 μC cm^{-2}) is approximately equivalent to the sum of the integrated charge densities of the ASV peaks II and IV in $(Ni\text{-}MoS_2)_{1000}$ nanoclusters, ascribed to the Ni-doped and Ni-undoped Mo-edge sites, respectively (Ni-doped Mo-edge sites peak II: $\langle\sigma_q\rangle$ approximately 13.4 μC cm^{-2}, undoped Mo-edge sites peak IV: $\langle\sigma_q\rangle$ approximately 14.3 μC cm^{-2}, total charge density originated by Mo-edge sites: $\langle\sigma_q\rangle$ approximately 27.7 μC cm^{-2}). Differences observed are correlated with variations in the nanoclusters loading as well as peak integration.

Peak III in $(Ni\text{-}MoS_2)_{1000}$ nanoclusters, ascribed in this manuscript as the electro-oxidative feature of the Ni-doped S-edge sites, was initially electrocatalytically inert and thus contributed to the ASV basal plane peak acquired for the $(MoS_2)_{300}$ nanoclusters.

The possibility of one of the peaks being due to the oxidation of a nickel sulfide species formed by interaction of Ni and MoS_2 nanoclusters can be easily discarded by the peak positions: this process occurs at potentials ca. −0.05 V, out of our electrochemical window.[49]

This peak identification also provides some insight on the thermodynamic stability of Ni-doped Mo-edge and S-edge sites. Analogous to nondoped MoS_2 nanoclusters, the lower oxidation potential of peak II with respect to peak III would imply that the Ni-doped Mo-edge sites are more thermodynamically unstable than the Ni-doped S-edge sites. Kibsgaard et al. observed that M (M = Fe, Co, Ni, Cu) doped-MoS_2 nanoparticles prepared by physical vapor deposition exhibited, in terms of $(\bar{1}010)$ S-edge and $(10\bar{1}0)$ Mo-edge relative free energies, stabilized S-edge sites in MoS_2 with respect to Mo-edge sites, in agreement with the peak position order experimentally observed in the ASV.[14]

CONCLUSIONS

$Ni\text{-}MoS_2$ hybrid nanoclusters have been successfully fabricated by dual target magnetron sputtering and gas condensation deposition, obtaining a unimodal size distribution with an average cluster size of 1000 equiv MoS_2 subunits. EDX mapping on the AC-STEM images confirm that the resulting nanoclusters are a hybrid of Ni and MoS_2 rather than their segregated components. The activity of $Ni\text{-}MoS_2$ hybrid nanoclusters is on par with previous reports of electrocatalytic enhancement to HER: an almost 3-fold increase in exchange current densities along with a significant shift in the onset potential (approximately 100 mV), as well as an almost unaffected Tafel slope (≈ 120 mVdec^{-1}). This activity is only achieved when nanoclusters are exposed to atmospheric environment, suggesting that only when Ni dopant atoms/aggregates oxidize will the Ni-doped edge sites become fully HER active, which is supported by XPS measurements. Anodic stripping voltammetry experiments revealed that HER-active undoped and doped edge sites are electrochemically distinguishable according to their thermodynamic stability, following the order Ni-doped Mo-edge< Ni-doped S-edge< pristine Mo-edge. The successful electrochemical identification of S-edge doping and its subsequent correlation with the HER enhancement confirm the capability of dual target magnetron sputtering and gas condensation deposition technique for the preparation of TM-doped TMDs. Finally, anodic stripping voltammetry is a powerful technique for probing TM-doped TMDs and tailoring doping parameters.

ASSOCIATED CONTENT

Supporting Information

The Supporting Information is available free of charge on the ACS Publications website at DOI: 10.1021/acscatal.6b01274.

Additional experimental details, calculations of $Ni\text{-}MoS_2$ cluster composition, estimation of surface coverages, calculation of turnover frequencies, and additional electrochemical results (PDF)

AUTHOR INFORMATION

Corresponding Authors

*E-mail for N.V.R.: n.rees@bham.ac.uk.
*E-mail for R.E.P.: r.e.palmer@bham.ac.uk

Author Contributions

The manuscript was written through contributions of all authors. All authors have given approval to the final version of the manuscript.

Notes

The authors declare no competing financial interest.

ACKNOWLEDGMENTS

The authors thank the EPSRC for support through a fellowship (to R.E.P.) and funding for the Centre for Doctoral Training in Fuel Cells and their fuels (to D.E.L., N.V.R.), as well as the European Research Council Marie-Curie ITN "Catsense" (to Y.N., J.Y., K.C.). The authors would also like to thank Mr. James Hunns and Dr. Mark Isaacs at the European Bioenergy Research Institute (Aston University, Birmingham) for the XPS measurement acquisition.

REFERENCES

(1) Jaramillo, T. F.; Jørgensen, K. P.; Bonde, J.; Nielsen, J. H.; Horch, S.; Chorkendorff, I. *Science* **2007**, *317*, 100−103.
(2) Voiry, D.; Salehi, M.; Silva, R.; Fujita, T.; Chen, M.; Asefa, T.; Shenoy, V. B.; Eda, G.; Chhowalla, M. *Nano Lett.* **2013**, *13*, 6222−6227.
(3) Chen, Z.; Cummins, D.; Reinecke, B. N.; Clark, E.; Sunkara, M. K.; Jaramillo, T. F. *Nano Lett.* **2011**, *11*, 4168−4175.
(4) Kibsgaard, J.; Chen, Z.; Reinecke, B. N.; Jaramillo, T. F. *Nat. Mater.* **2012**, *11*, 963−969.
(5) Li, Y.; Wang, H.; Xie, L.; Liang, Y.; Hong, G.; Dai, H. *J. Am. Chem. Soc.* **2011**, *133*, 7296−7299.
(6) Hinnemann, B.; Moses, P.; Bonde, J.; Jørgensen, K. P.; Nielsen, J. H.; Horch, S.; Chorkendorff, I.; Nørskov, J. K. *J. Am. Chem. Soc.* **2005**, *127*, 5308−5309.
(7) Shi, Y.; Wan, Y.; Liu, R.; Tu, B.; Zhao, D. *J. Am. Chem. Soc.* **2007**, *129*, 9522−9531.

DOI: 10.1021/acscatal.6b01274
ACS Catal. 2016, 6, 6008−6017

(8) Zhu, H.; Du, M.; Zhang, M.; Zou, M.; Yang, T.; Wang, S.; Yao, J.; Guo, B. *Chem. Commun.* **2014**, *50*, 15435−15438.
(9) Benck, J. D.; Hellstern, T. R.; Kibsgaard, J.; Chakthranont, P.; Jaramillo, T. F. *ACS Catal.* **2014**, *4*, 3957−3971.
(10) Tsai, C.; Chan, K.; Nørskov, J. K.; Abild-Pedersen, F. *Catal. Sci. Technol.* **2015**, *5*, 246−253.
(11) Bonde, J.; Moses, P. G.; Jaramillo, T. F.; Norskov, J.; Chorkendorff, I. *Faraday Discuss.* **2009**, *140*, 219−231.
(12) Merki, D.; Vrubel, H.; Rovelli, L.; Fierro, S.; Hu, X. *Chem. Sci.* **2012**, *3*, 2515.
(13) Wang, H.; Tsai, C.; Kong, D.; Chan, K.; Abild-Pedersen, F.; Nørskov, J. K.; Cui, Y. *Nano Res.* **2015**, *8*, 566−575.
(14) Kibsgaard, J.; Tuxen, A.; Knudsen, K. G.; Brorson, M.; Topsøe, H.; Lægsgaard, E.; Lauritsen, J. V.; Besenbacher, F. *J. Catal.* **2010**, *272*, 195−203.
(15) Lauritsen, J.; Kibsgaard, J.; Olesen, G.; Moses, P.; Hinnemann, B.; Helveg, S.; Norskov, J.; Clausen, B.; Topsoe, H.; Lagsgaard, E. *J. Catal.* **2007**, *249*, 220−233.
(16) Cuddy, M. J.; Arkill, K. P.; Wang, Z. W.; Komsa, H.-P.; Krasheninnikov, A. V.; Palmer, R. E. *Nanoscale* **2014**, *6*, 12463−12469.
(17) Xu, C.; Peng, S.; Tan, C.; Ang, H.; Tan, H.; Zhang, H.; Yan, Q. *J. Mater. Chem. A* **2014**, *2*, 5597−5601.
(18) Eng, A. Y. S.; Ambrosi, A.; Sofer, Z.; Simek, P.; Pumera, M. *ACS Nano* **2014**, *8*, 12185−12198.
(19) Ellis, P.; Brown, C. M.; Bishop, P. T.; Yin, J.; Cooke, K.; Terry, W. D.; Liu, J.; Yin, F.; Palmer, R. E. *Faraday Discuss.* **2016**, *188*, 39.
(20) Wang, Z. W.; Li, Z. Y.; Park, S. J.; Abdela, A.; Tang, D.; Palmer, R. E. *Phys. Rev. B: Condens. Matter Mater. Phys.* **2011**, *84*, 2−4.
(21) Brown, N. M. D.; Cui, N.; Mckinley, A. *Appl. Surf. Sci.* **1998**, *134*, 11−21.
(22) Grunert, W.; Stakheev, A. Y.; Feldhaus, R.; Anders, K.; Shpiro, E. S.; Minachev, K. M. *J. Phys. Chem.* **1991**, *95*, 1323−1328.
(23) Baker, M. A.; Gilmore, R.; Lenardi, C.; Gissler, W. *Appl. Surf. Sci.* **1999**, *150*, 255−262.
(24) Escalera-López, D.; Gómez, E.; Vallés, E. *Phys. Chem. Chem. Phys.* **2015**, *17*, 16575−16586.
(25) Benck, J. D.; Chen, Z.; Kuritzky, L. Y.; Forman, A. J.; Jaramillo, T. F. *ACS Catal.* **2012**, *2*, 1916−1923.
(26) Biesinger, M. C.; Payne, B. P.; Lau, L. W. M.; Gerson, A.; Smart, R. S. C. *Surf. Interface Anal.* **2009**, *41* (4), 324−332.
(27) Grosvenor, A. P.; Biesinger, M. C.; Smart, R. S. C.; McIntyre, N. S. *Surf. Sci.* **2006**, *600*, 1771−1779.
(28) Jiang, N.; Tang, Q.; Sheng, M.; You, B.; Jiang, D.; Sun, Y. *Catal. Sci. Technol.* **2016**, *6*, 1077−1084.
(29) Jiang, N.; Bogoev, L.; Popova, M.; Gul, S.; Yano, J.; Sun, Y. *J. Mater. Chem. A* **2014**, *2*, 19407−19414.
(30) Lukowski, M. A.; Daniel, A. S.; Meng, F.; Forticaux, A.; Li, L.; Jin, S. *J. Am. Chem. Soc.* **2013**, *135*, 10274−10277.
(31) Thakurta, S. R. G. *Indian J. Phys.* **1969**, *43*, 169−172.
(32) Burch, H. A.; Isaacs, M.; Wilson, K.; Palmer, R. E.; Rees, N. V. *RSC Adv.* **2016**, *6*, 26689−26695.
(33) Xie, S.; Xu, M.; Liang, T.; Huang, G.; Wang, S.; Xue, G.; Meng, N.; Xu, Y.; Chen, H.; Ma, X.; Yang, D. *Nanoscale* **2016**, *8*, 219−225.
(34) Lauritsen, J. V.; Bollinger, M. V.; Lægsgaard, E.; Jacobsen, K. W.; Nørskov, J. K.; Clausen, B. S.; Topsøe, H.; Besenbacher, F. *J. Catal.* **2004**, *221*, 510−522.
(35) Vrubel, H.; Hu, X. *ACS Catal.* **2013**, *3*, 2002−2011.
(36) Rowley-Neale, S. J.; Brownson, D. A. C.; Smith, G. C.; Sawtell, D. A. G.; Kelly, P. J.; Banks, C. E. *Nanoscale* **2015**, *7*, 18152−18168.
(37) Gao, M.-R.; Liang, J.-X.; Zheng, Y.-R.; Xu, Y.-F.; Jiang, J.; Gao, Q.; Li, J.; Yu, S.-H. *Nat. Commun.* **2015**, *6*, 5982.
(38) Yu, Y.; Huang, S. Y.; Li, Y.; Steinmann, S. N.; Yang, W.; Cao, L. *Nano Lett.* **2014**, *14*, 553−558.
(39) Chia, X.; Ambrosi, A.; Sofer, Z.; Luxa, J.; Pumera, M. *ACS Nano* **2015**, *9*, 5164−5179.
(40) Gao, M.-R.; Chan, M. K. Y.; Sun, Y. *Nat. Commun.* **2015**, *6*, 7493.
(41) Navarro-Flores, E.; Chong, Z.; Omanovic, S. *J. Mol. Catal. A: Chem.* **2005**, *226*, 179−197.
(42) Medway, S. L.; Lucas, C. a.; Kowal, a.; Nichols, R. J.; Johnson, D. *J. Electroanal. Chem.* **2006**, *587*, 172−181.
(43) Subbaraman, R.; Tripkovic, D.; Strmcnik, D.; Chang, K.-C.; Uchimura, M.; Paulikas, A. P.; Stamenkovic, V.; Markovic, N. M. *Science* **2011**, *334*, 1256−1260.
(44) Thiel, P. A.; Madey, T. E. *Surf. Sci. Rep.* **1987**, *7*, 211−385.
(45) Kautek, W.; Gerischer, H. *Surf. Sci.* **1982**, *119*, 46−60.
(46) Schweiger, H.; Raybaud, P.; Toulhoat, H. *J. Catal.* **2002**, *212*, 33−38.
(47) Deng, J.; Li, H.; Xiao, J.; Tu, Y.; Deng, D.; Yang, H.; Tian, H.; Li, J.; Ren, P.; Bao, X. *Energy Environ. Sci.* **2015**, *8*, 1594−1601.
(48) Li, H.; Tsai, C.; Koh, A. L.; Cai, L.; Contryman, A. W.; Fragapane, A. H.; Zhao, J.; Han, H. S.; Manoharan, H. C.; Abild-Pedersen, F.; Nørskov, J. K.; Zheng, X. *Nat. Mater.* **2015**, *15*, 48−53.
(49) Giovanelli, D.; Lawrence, N. S.; Wilkins, S. J.; Jiang, L.; Jones, T. G. J.; Compton, R. G. *Talanta* **2003**, *61*, 211−220.

DOI: 10.1021/acscatal.6b01274
ACS Catal. 2016, 6, 6008−6017